Combined membrane potential imaging and connectome of behavioral circuits in an annelid worm

Mária Ashaber[1*], Yusuke Tomina[1,2*], Pegah Kassraian-Fard[1*], Eric A. Bushong[3], William B. Kristan Jr[3], Mark H. Ellisman[4,5] and Daniel A. Wagenaar[1+]

1 Division of Biology and Biological Engineering, California Institute of Technology, Pasadena, CA, USA.

2 Faculty of Science and Technology, Keio University, Yokohama, Kanagawa, JAPAN.

3 Division of Biological Sciences, University of California, San Diego, La Jolla, CA, USA.

4 National Center for Microscopy and Imaging Research, University of California, San Diego, La Jolla, CA, USA.

5 Department of Neurosciences, UCSD School of Medicine

* These authors contributed equally.

\+ Correspondence: Caltech 139-74, Pasadena, CA 91125, USA; daw@caltech.edu; ++1-626-395-8567.

Abstract

In most animal phyla, nerve cells form highly specific connections with each other[1,2]. The resulting intricate networks determine what activity patterns a nervous system can sustain, and hence what behaviors an animal can exhibit[3,4]. Accordingly, understanding the relationship between connectivity and activity is a major goal of neuroscience. However, despite major recent advances[5,6], no current technology can comprehensively record activity in large nervous systems such as the human or even the mouse brain, nor can connectivity be reconstructed at synaptic level in such systems[7]. Doing both at once in the same specimen remains a distant goal.

However, smaller nervous systems offer exciting opportunities today, and here we report for the first time obtaining joint functional and anatomical data from a major functional unit of the nervous system of the medicinal leech, by combining voltage-sensitive dye (VSD)[8] imaging with serial blockface electron microscopy (SBEM)[9]. We simultaneously recorded from the majority of the neurons in a segmental ganglion during several motor behaviors with a VSD sufficiently sensitive to record subthreshold neuronal activity[10,11]. We then anatomically imaged the entire ganglion with SBEM[12]. As a proof of concept, we have manually traced a critical motor neuron and identified all of its numerous presynaptic partners. The thorough reconstruction of individual synapses in combination with functional data enabled a quantitative analysis that revealed spatial clustering of synapses from functionally synchronized cell assemblies. All of our data is publicly available.

Main

Understanding the relationship between connectivity and activity in the nervous system remains one of the great intellectual challenges in science and it requires the integration of functional and anatomical approaches. In the age of large-scale "omics" projects, one would ideally like to record from every single neuron in a nervous system during all of the behaviors the animal can execute, and then reconstruct the anatomical connections between those neurons. Although still monumental, neither of these endeavors is out of reach anymore: Activity imaging using calcium dyes has advanced to the point where simultaneous recordings from the vast majority of individual neurons in smaller species can be accomplished, for instance in larval zebrafish[5]. This technique has even been applied to behaving animals[13]. Likewise, anatomical imaging using electron microscopy has advanced to the point that brains as large as that of the fruit fly *Drosophila melanogaster* can be imaged—and substantial fractions of their circuitry reconstructed—at a synaptic resolution[6,14,15,16]. Even small mammalian brains like that of larval zebrafish are yielding to this approach[17].

Critically, however, robustly linking function to connectivity requires a combined anatomical and functional assessment within the same animal. After all, even the simplest nervous systems exhibit some variability in their connectomes[18] (and larger ones exponentially more). Yet, each of the studies mentioned above addressed either function (by recording neuronal activity) or connectivity (by reconstructing anatomy) in isolation. Here we performed for the first time a combined assessment by first recording with a voltage-sensitive dye (VSD)[19] from a segmental ganglion of the medicinal leech *Hirudo verbana* while its nervous system expressed several behaviors and then imaging the same individual ganglion with serial blockface electron microscopy (SBEM; Fig. 1). A leech segmental ganglion is a good stand-in for a whole nervous system, because its neurons capture the entire pathway from sensory input through self-generated interneuronal rhythms to motor output. We chose VSD imaging over calcium imaging for this pioneering study, because VSDs can detect both action potentials and subthreshold excitatory and inhibitory potentials. Likewise, we chose SBEM over serial-section transmission EM[20] because SBEM can reliably process large numbers of slices with much lower risk of sectioning artifacts. Lastly, we chose the leech for this study because it robustly expresses several behaviors even in reduced preparations[21], its neurons are uncommonly accessible to physiological recording, and its cell bodies are relatively large and thus yield strong VSD signals[22]. The nervous system of the leech comprises cephalic ganglia, a tail ganglion, and 21 nearly identical segmental ganglia connected by a ventral nerve cord[23,24]. We focused on the segmental ganglia, because those are largely responsible for processing sensory information and generating muscle activity[21].

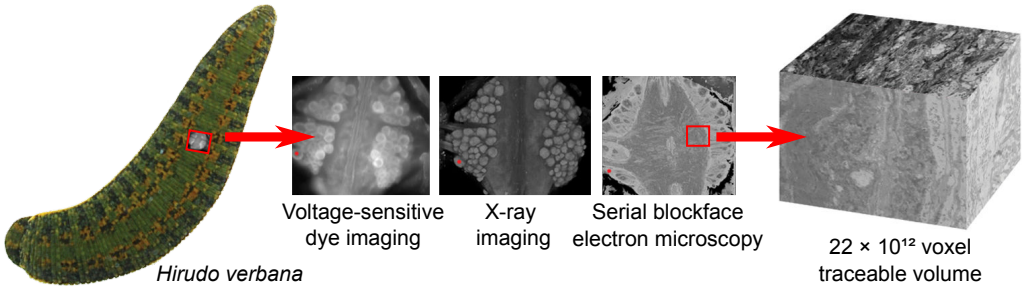

Figure 1: Approach. Several fictive behaviors were induced in the isolated nervous system of a medicinal leech while one segmental ganglion was imaged using a VSD. After fixation and resin embedding, the ganglion was x-ray-imaged to verify that the geometry of somata was preserved. Finally, the neuropil was imaged at nanometer resolution with SBEM.

Voltage-dye imaging of behavior

Each ganglion consists of about 400 neurons[25] with cell bodies arranged in a spherical monolayer around a central neuropil. In the neuropil, neurons communicate through chemical and electrical synapses located along extensively branched neurites[26,27,12]. Unlike in mammals, leech neuronal processes cannot be subdivided into axons and dendrites.

We expressed (fictive) swimming, crawling, and local bending behavior in the isolated nervous system of a single leech following the same protocol used for a previous extensive study of these behaviors using VSD imaging in a larger group of animals[11]. As in the previous study, one segmental ganglion in the chain was prepared for VSD imaging and we recorded from both the ventral and dorsal aspects simultaneously with a double-sided fluorescence microscope (Fig. 2a). We were able to record from 250 neurons simultaneously, similar to our previous results. Fictive swimming was induced by electrical stimulation of a posterior segment, which resulted in characteristic rhythmic activity in dorsal motor neurons and many other neurons on both sides of the ganglion (Fig. 2b). Coherence analysis confirmed that the rhythms of the various neurons were indeed related (Fig. 2c, d). In a similar manner, we induced fictive local bending (Fig. S1) and crawling (Fig. S2).

We established a mapping between the neurons seen in the VSD images and the canonical maps of the ganglion[28] based on geometry and on the involvement of the neurons in the various behaviors.

Electron microscopy

At the end of the (fictive) behavior experiment, the ganglion was fixated and embedded in a resin. We then re-imaged the ganglion using x-ray tomography and verified that the cell bodies seen in the VSD images could still be identified (Fig. S3a). The x-ray image stack was also used to trace neuronal processes from the somata to the edge of the neuropil (Fig. S3b). This obviated the need to capture the somata in the subsequent electron microscopy, and instead allowed us to restrict the

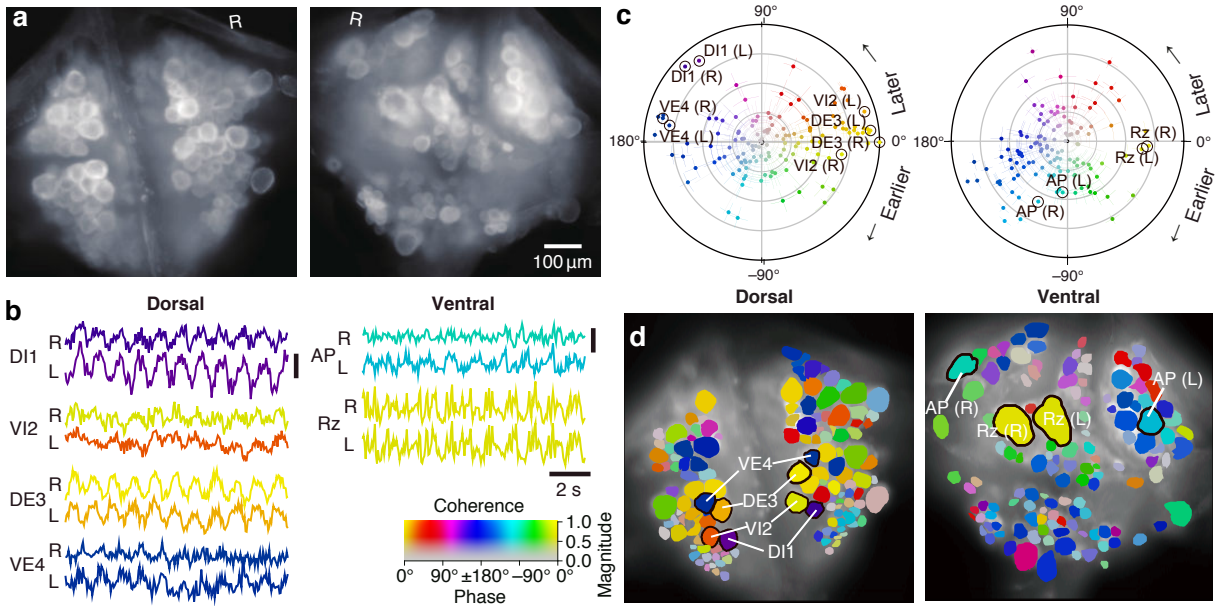

Figure 2: Fictive swimming imaged using VSD. **a**. Images of the dorsal (*left*) and ventral (*right*) aspects of a leech ganglion simultaneously obtained using a double-sided microscope. "R" indicates the right side of the ganglion (i.e., the animal's right when dorsal side up). **b**. Selected VSD traces during fictive swimming. From the dorsal surface: dorsal and ventral inhibitory and excitatory motor neurons DI-1, VI-2, DE-3, and VE-4; from the ventral surface: AP ("Anterior Pagoda") cells and the Retzius cells (neuromodulatory interneurons). Vertical scale bars: 0.2% relative fluorescence change **c**. Magnitude (radial axis from 0 to 1) and phase (angular coordinate) of the coherence of activity in individual neurons with the swim rhythm. Error bars indicate confidence intervals based on a multi-taper estimate. **d**. Coherence maps of the VSD signals of all cells on the dorsal (*left*) and ventral (*right*) surfaces of the ganglion. Colors of cell bodies indicate coherence relative to excitatory motor neuron DE-3^{R}. Color scale applies to all panels.

EM effort largely to the neuropil.

Electron microscopy itself took nearly 7 months of imaging, during which we acquired 78,803 images from 9604 slices, totaling 22.8 terapixels. We periodically paused the acquisition to clean the knife or to adjust the imaging area so as to include the entirety of the neuropil but not too much additional space.

Tracing a motor neuron and all its synaptic inputs

With current technology, automated tracing of the fine processes in our EM image set was not possible. Therefore we decided to manually trace one motor neuron of particular interest and all of its presynaptic inputs. The motor neuron we chose was Dorsal Excitor motor neuron DE-3^{R}, a common output of all of the behaviors included in our functional data set. The combined path length of the entire arborization of DE-3^{R} was 6,109 µm (Fig. 3a, b, c).

In addition to tracing the neuron, we marked all of its postsynaptic sites and then traced each of its presynaptic partners to their somata. Several visually distinct types of synapses were

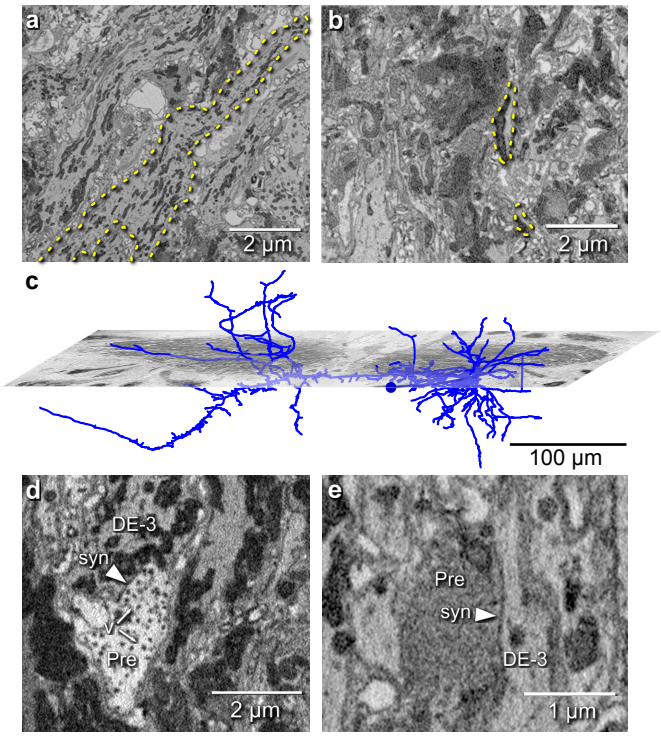

Figure 3: Electron microscopic tracing: neurites and synapses of motor neuron DE-3^R. **a**. The principal neurite of DE-3^R near its entrace to the neuropil (*dashed yellow outline*). **b**. Two branches of the neurite of DE-3^R (*dashed outlines*). **c**. Fully reconstructed arborization of DE-3^R with a transverse section of the ganglion. (In the perspective, anterior is up, dorsal is near.) **d**. A synaptic connection onto DE-3^R from an inhibitory motor neuron (DI-1^R). Arrowheads: synapses, Pre: presynaptic terminal, v: vesiscles. **e**. A synapse onto DE-3^R from an interneuron (cell 24 on the canonical map[28]).

found, among which most prominently: (1) bright terminals with large dark vesicles (Fig. 3d) and (2) darker terminals with smaller vesicles that occurred mainly in fiber endings and varicosities (Fig. 3e). The small vesicles are barely resolved in our data set and appear merely as fields of granules. We used TEM on thin slices of a second ganglion to confirm our interpretation of these granules as vesicles (Fig. S4). No attempt has been made as of yet to interpret the anatomically distinct types of synapses as physiological classes.

We identified 531 synapses onto DE-3^R. Of these, 44 were formed by cells with somata in neighboring ganglia, which were not included in our EM volume. Of the rest, 387 could be traced to their somata with a high degree of confidence. To avoid false positives, we only considered presynaptic neurons that formed at least two synapses onto DE-3^R. There were 51 of those. Of those, 27 could be confidently matched to cell bodies seen in the VSD record, and of those, 14 could be confidently matched to specific identified neurons on the canonical map (Fig. 4a).

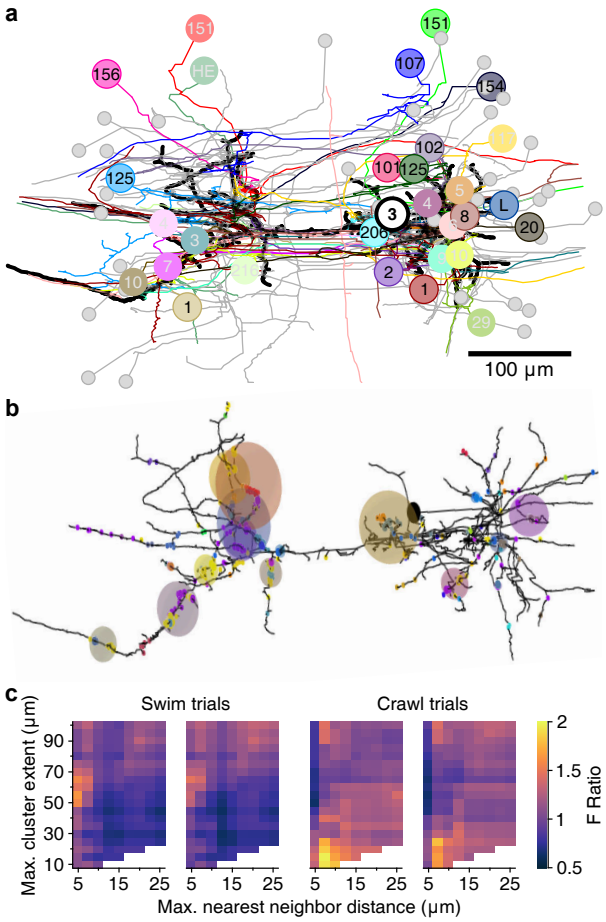

Figure 4: Partner neurons of DE-3^R with multiple synapses. **a**. Full tracing of DE-3^R (thick black line, soma location marked by boldface "3") and backtracings of all synaptic partners. Partners that we could identify as known entities on the canonical ganglion map are colored (arbitrarily) and labeled in black type for confident identification, light gray type for low-confidence partners. Small gray disks indicate partner neurons that could not be cross-identified between EM and VSD imagery. **b**. Tracing of DE-3^R with synapses and synaptic clusters obtained with parameter values (d_{NN}, e_C) = (5 µm, 65 µm). Synapses (small dots) are colored by the coherence between the activity of their presynaptic partner and DE-3^R during swimming (as in Fig. 2). Clusters (elliptic areas) are colored by the average coherence of their constituent presynaptic partners. **c**. All clustering results for swim and crawl trials. Color indicates the degree of correspondence between spatial clusters and functional grouping expressed as an F-ratio from complex ANOVA (see Methods) as a function of clustering parameters.

Linking form to function: Synaptic clustering

Spatial clustering of synapses on the dendrites of a neuron has been proposed as a key organizational principle of circuits that integrate multiple sources of information[29,30,31]. Since motor neuron DE-3^R must integrate input from its presynaptic partners to accurately generate multiple behaviors, we therefore assessed the spatial distribution of synapses on the neurites of DE-3^R. Cluster analysis (Fig. 4b) revealed a multitude of synaptic clusters. Most clusters contained synapses from

multiple partner neurons.

A key strength of our dataset is that it contains both functional and anatomical information. Accordingly, we were able to assess the functional relevance of these spatially defined synaptic clusters by investigating whether neurons that contribute synapses to a specific cluster share commonalities in their activity during behaviors. An ANOVA-style procedure was used that yielded an F-ratio indicating whether coherence values of neurons were more similar within spatial clusters than between clusters. The procedure was applied to each of the trials separately and for a range of clustering parameters (see Methods). In all but one trial, parameter ranges could be identified for which spatial clusters were found to correspond to functional groupings (Fig. 4c and Fig. S5). We used a least-squares fit approach to find the location in parameter space of the strongest correspondence (Fig. S6 and Methods). In the two swim trials, the peaks were located at $e_C = 61 \pm 2$ µm and 65 ± 2 µm respectively; in the two crawl trials at 14 ± 5 µm and 18 ± 3 µm. In summary, the clustering parameters that led to the strongest correspondence in swim trials were quite different compared to crawl trials, but consistent within a trial type. (Results for local bend trials were not consistent; Fig. S5).

Conclusion

We successfully combined voltage-sensitive dye imaging with serial-blockface electron microscopy to obtain both detailed functional and anatomical information from the same individual nervous system. For this purpose we chose a segmental ganglion from the medicinal leech *Hirudo verbana* which contains the neuronal circuits that support motor behaviors including swimming, crawling, and local bending. After functional and anatomical imaging, we focused on the reconstruction of the main excitatory motor neuron of dorsal longitudinal muscles, DE-3^R along with its presynaptic partners[32].

The reconstructed morphology of the motor neuron DE-3^R was in accordance with previous light microscopic studies in adult[33,27] and electron microscopy in a juvenile ganglion[12]: its primary neurite emerged from the soma laterally and traveled toward the ipsilateral roots before making a 180° turn to run laterally across the ganglion. We could positively identify the EM image of the soma of DE-3^R with its image in VSD data (Fig. S3). Our tracing revealed 531 synapses onto DE-3^R. This was slightly lower than the number previously reported for a juvenile ganglion (650)[12]. The difference may be due to individual variability or developmental plasticity. Several of the synapses we found were with presynaptic partners that had previously been reported[34] based on paired electrophysiological recordings. We focused here on chemical synaptic connections, since SBEM does not yet allow identification of gap junctions. Work on molecular markers of electrical synapses that do not require expression of a particular connexin[35] may overcome this hurdle in the future. This is important, because electrical synapses between DE-3 and their contralateral homologs as well as some interneurons have been reported[27].

Motor neuron DE-3 and its presynaptic partners form a multifunctional neuronal circuit; DE-3 being a common output for multiple motor behaviors. Combining VSD and SBEM data allowed for an integrated assessment of structure and function of this circuit: First, the detailed anatomical reconstruction at synaptic level revealed the local convergence of presynaptic cells within synaptic clusters on the neurites of the motor neuron. Second, referring back to the VSD results showed that these clusters act as functionally cohesive units. That is, anatomically defined clusters tended to comprise presynaptic partners with like activity patterns in the behaviors we studied. An attractive interpretation of our results is that the clusters are the loci where inputs from synchronized presynaptic cell assemblies are integrated[36]. The limited experimental evidence currently available suggests that even clusters of two synapses are functionally relevant in the mammalian cortex[29,37]. In agreement with earlier reports[38], the strongest correspondence between spatial clusters and activity patterns was observed when synaptic clusters were defined by a maximum distance between nearest neighbors (d_{NN}) of up to 10 µm. In contrast to earlier work that relied on light microscopy and could therefore not identify presynaptic partners, our use of SBEM allowed us to base our assessment directly on individually identified synapses.

All of our data are publicly available and can form the basis of future investigations of the relationship between form and function in nervous systems. They can also serve as a large-scale ground truth for EM segmentation algorithms[39]. The combination of anatomical methods with synaptic resolution and imaging techniques that can record from the entirety of the neurons of a circuit promises an extraordinary opportunity to assess neural computations at the level of circuit dynamics. Functional maps[40] from recorded activity combined with anatomical connectomes[41,42,43] are therefore poised to become a powerful tool not only to have a better understanding of complex behaviors, but also to predict the outcomes of new manipulations[44,45,46].

Methods

Dissection and voltage-sensitive dye imaging

Detailed procedures have been described before[47]. Briefly, leeches (*Hirudo verbana*, obtained from Niagara Leeches, Niagara Falls NY) were maintained on a 12h:12h light:dark cycle in temperature-controlled aquariums filled with artificial pond water. The entire nervous system of a leech was removed and pinned down on silicone (PDMS, Sylgard 184, Dow Corning, Midland, MI). The sheath surrounding one segmental ganglion (M10) was removed from both ventral and dorsal aspects to allow access with voltage-sensitive dyes. Most of the nerves that innervate the periphery were cut short, but several were kept long to allow extracellular stimulation as described before[11]. A voltage-sensitive dye (VF2.1(OMe).H[48] provided by Evan Miller) was bath-loaded at a concentration of 800 nM in leech saline using a pair of peristaltic pumps to evenly load cell membranes on both sides of the ganglion. The preparation was placed on a custom-built dual-headed microscope which was used to image neuronal activity during fictive behaviors triggered by electrical

stimulation, as in our previous work[11].

We manually drew regions of interest (ROIs) around neuronal cell bodies and used custom software to associate those ROIs with named cells on the canonical maps of the leech ganglion[28]. For each of the behavior trials separately, we calculated the spectral coherence between each of the neurons and DE-3^R at the frequency of the dominant peak in the power spectrum of DE-3^R for the given behavior.

Histology

After dye imaging, the preparation was reduced to just one segmental ganglion by transecting the anterior and posterior connectives. The ganglion was mounted on a slab of silicone (DPMS) with a hole cut out in the center so that the somata would not be in direct contact with the silicone. This preparation was transferred into a glass container and incubated for 72 hours at 4 °C in 2% paraformaldehyde, 2.5% glutaraldehyde in 0.15 M cacodylate buffer containing 2 mM $CaCl_2$. Subsequently, the ganglion was washed in cacodylate buffer for 10 minutes and then incubated in an aqueous solution of 2% OsO_4 and 1.5% potassium ferrocyanide. During this incubation, the sample was microwaved in a scientific microwave (Pelco 3440 MAX) three times at 800 W with a duty cycle of 40 seconds on and 40 seconds off at a controlled temperature of 35 °C and subsequently left at room temperature (RT) for 30 minutes. The sample was then washed twice in ddH_2O and then microwaved three times at 30 °C with a duty cycle of 2 minutes on and 2 minutes off.

The sample was incubated in 0.5% thiocarbohydrazide (Electron Microscopy Sciences, Hatfield, PA). During this incubation, the sample was microwaved three times at 800 W with a duty cycle of 40 seconds on and 40 seconds off at 30 °C and subsequently left at RT for 15 minutes. The ganglion was then washed again, followed by the same microwave incubation as described above.

Next, the sample was incubated in 2% aqueous OsO_4, microwaved three times at 800 W with a duty cycle of 40 seconds on and 40 seconds off at 30 °C, and left for 30 minutes at RT. After another wash, the sample was left overnight in 2% uranyl acetate at 4 °C.

The next day, the sample was incubated in a lead aspartate solution at 60 °C for 25 minutes[49]. The sample was then washed and dehydrated through a series of ethanol solutions (50%, 70%, 90%, 100%, 100%, 10 minutes each) at RT and incubated in acetone. After this, the sample was infiltrated with epoxy resin by first incubating it for one day at RT in a solution of 25% Durcupan (Sigma, St. Louis, MO) in acetone. On subsequent days, the concentration of Durcupan was increased to 50%, 75%, and finally 100%. After that, the sample was transferred to freshly prepared 100% Durcupan and incubated at 60 °C for 3 days.

Micro-CT Imaging

We used Micro-CT scanning to confirm that the above sample preparation had left the overall geometry of the ganglion intact and to trace portions of neurons outside of the neuropil. Scans were collected using the 20x objective on a Zeiss Versa 510 X-ray microscope. Epoxy-embedded ganglia were attached to the end of an aluminum rod using cyanoacrylate glue and then scanned at 80 kV, collecting 2401 projection images while rotating the specimen 360 degrees. The final pixel size was approximately 0.75 µm. Volumes were reconstructed using Zeiss Reconstructor software and visualized in custom software (GVox, see "Data availability").

Scanning electron microscopy

Ganglia were mounted onto aluminum pins using conductive silver paint. The ganglia were mounted in a vertical orientation (with the anterior connective pointing upwards). The sample was imaged with a Zeiss Gemini 300 SEM with a Gatan 2XP 3View system. The microscope was run in focal charge compensation mode using nitrogen gas (40% pressure), with an accelerating voltage of 2.5 kV, a 30 µm objective aperture, magnification of 336x, a raster size of 17100 × 17100 pixels, a 5.5 nm pixel size, a 0.5 µs dwell time, and 50 nm section thickness. Stage montaging with an overlap of 8% between tiles was used to cover the complete extent of the ganglion in any given image. The backscatter detector was a Hamamatsu diode with a 2-mm aperture.

Outside of the neuropil, neuronal processes could be traced in the micro-CT scan, which allowed us to reduce the total volume needed to be imaged with SBEM by almost a factor two (Figure S3b). Still, at the widest points of the neuropil as many as 7 × 2 tiles (119,700 × 34,200 pixels) were needed at a given z-position.

After approximately every 500 sections, the run was stopped to clear sectioning debris from the diamond knife and prevent contamination of the block-face, diode, or column. The run was also stopped when we reached significantly wider or narrower regions of the neuropil as indicated above. Ultimately, the run was subdivided into 61 subruns. There was only one instance in the run where a significant loss of tissue occurred (approximately 150 nm) following the re-approach of the knife to the tissue after an interruption for clearing debris.

Transmission electron microscopy

Image quality and specimen preservation was verified using an additional ganglion prepared as above, but imaged in ultrathin sections on a conventional transmission electron microscope (JEOL JEM-1200EX, 120 kV, 12,000x–20,000x magnification).

Image processing

Images were aligned using custom software. First, we reduced the linear resolution of the original images by a factor five. Then we split each image into 5x5 sub-tiles and calculated the optimal

alignment between each sub-tile and the corresponding sub-tile from the image above using a modified version of SWIFT-IR[50]. Likewise, we split the regions of overlap that existing between images of the same slice into 5 sub-tiles and calculated the optimal alignment between the edges of adjacent images. We used these latter numbers to coarsely align images within each slice and render the first and last slices of each subrun at 1:25 scale, which allowed us to establish regions of correspondence between subruns. Using these procedures, we ended up with 3,430,650 matching pairs of image locations. Because SWIFT-IR matches up entire areas rather than single point pairs, those locations are defined at a much higher resolution than that of the images. Accordingly, alignment information obtained at a scale of 1:5 could be used to align the source images at scale 1:1 without material loss of precision.

Next, we split the full EM volume up into subvolumes of 200 slices with 50% overlap between subsequent subvolumes (Stefan Saalfeld, personal communication) and optimized alignment in each subvolume independently. This was done in three steps: (1) Coarse alignment of all the z-stacks from all of the subruns involved in the subvolume relative to each other; (2) Refinement of this alignment by determining optimal rigid translation of each tile relative to its substack; (3) Further refinement through elastic deformation. This procedure resulted in absolute coordinates for a grid of points in each source image.

We then rendered each slice by linearly combining the placement according to the two subvolumes that incorporated the slice. We divided each slice up into nonoverlapping rectangles and rendered pixels from one source image into each rectangle using a perspective transformation derived from the grid coordinates calculated in the previous step.

The full-resolution stitched volume was then split into tiles of 512x512x1 voxels and reduced-resolution tiles at 1:2, 1:4, up to 1:256 resolution were produced for faster online visualization.

Visualization

We developed a custom tool for visualizing the aligned images and for neurite tracing. SBEMViewer (see "Data availability") was used to visualize the slices as they came off the microscope to monitor image quality, and also for purposes of tracing neurites.

Neurite tracing

We produced a full skeleton tracing of the right DE-3 motor neuron and all of its presynaptic partners from the synapses to their somata. The following criteria were used to identify synapses:

1. Vesicles have to be evident on the presynaptic site;
2. Those vesicles have to be in immediate proximity of the putative synapse;
3. The pre- and postsynaptic cells must have membrane apposition across at least three sections (150 nm).

Because of limited resolution in our SBEM images, synaptic vesicles appear merely as gray granules (Fig. 3c,d), but fields of such granules were clearly distinct from other gray areas in the SBEM images. Comparison with digitally blurred TEM images (Fig. S4) confirmed this interpretation. We found that granular areas were concentrated in fiber endings and varicosities.

Synaptic clustering analysis

The analysis was based on data from the 45 synaptic partners of DE-3^{R} for which both anatomical as well as VSD recordings were available. We defined synaptic clusters using an agglomerative hierarchical clustering algorithm with two parameters:

(1) The maximum allowed distance between nearest neighbors (d_{NN});

(2) The maximum overall spatial extent of the cluster (e_{C}).

The algorithm began by treating each synapse as an individual cluster. Then, it iteratively joined the two clusters with minimum distance between their most proximal elements ("single-linkage" clustering). However, if a joint cluster would exceed the limit on overall spatial extent (e_{C}), its putative constituents were not joined. Aggregation stopped when no pairs of clusters were left with acceptable nearest-neighbor distance (i.e., less than d_{NN}) and acceptable joint spatial extent (i.e., less than e_{C}). All distances were measured along the neurites of DE-3^{R} rather than by Euclidean metric in the volume. We explored maximum nearest-neighbor distances between 5 and 25 µm, and maximum spatial extents between 10 and 100 µm. Clusters comprising only a single synapse were not considered for further analysis.

The analysis of functional significance of spatial clusters used an ANOVA-like procedure on the complex spectral coherence values of neurons within clusters relative to DE-3^{R}. As in ANOVA, we calculated sums of squares within and between clusters. Since coherence values are complex numbers, we used the *absolute* square value. In standard ANOVA, the ratio of these sums of squares (the "F-ratio") follows an F-distribution under the null hypothesis. In the complex-valued case, that is no longer true, so we calculated empirical distributions of the F-ratios by randomly shuffling the list of per-neuron coherence values 1000 times. The empirical p-value $\hat{p}$ was then defined as $\hat{p} = \frac{m+1}{N+1}$, where $N = 1000$ is the number of randomizations and m is the number of times the F-ratio from shuffled data exceeded the experimentally observed F-ratio. These p-values are reported in the supplemental table.

We generated plots of the F-ratio as a function of the cluster parameters d_{NN} and e_{C}. For each trial, we first determined the value of d_{NN} for which the largest F-ratio was obtained. Then, we fitted a Gaussian of the form

$$F = 1 + A \exp\left(-\frac{1}{2}[e_{\mathrm{C}} - \mu]^2/\sigma^2\right)$$

to the F-ratio as a function of e_{C} (Fig. S6). The μ-values from those fits and their uncertainties according to least-squares fitting are reported in the text.

Data availability

The easiest way to access the raw electrophysiology and voltage-dye data as well as the tracing results used in this paper is through a series of Python modules that we made available at `https://github.com/wagenadl/leechem-public`. Included in the package is a file called "demo.py" that demonstrates the use of the modules.

The aligned EM volume may be accessed through the Neuroglancer[51] instance at `https://leechem.caltech.edu` or by pointing SBEMViewer to `https://leechem.caltech.edu/emdata`.

The code used for alignment is available at `https://github.com/wagenadl/sbemalign`. Our visualization tools SBEMViewer and GVox are at `https://github.com/wagenadl/sbemviewer` and `https://github.com/wagenadl/gvox`.

References

[1] Yogev S and Shen K, 2014. Cellular and molecular mechanisms of synaptic specificity. *Annu Rev Cell Dev Biol* **30**: 417–437. PMID 25150010.

[2] Bielecki J and Garm A, 2018. Vision Made Easy: Cubozoans Can Advance Our Understanding of Systems-Level Visual Information Processing. *Results Probl Cell Differ* **65**: 599–624. PMID 30083938.

[3] O'Connell LA, 2013. Evolutionary development of neural systems in vertebrates and beyond. *J Neurogenet* **27** (3): 69–85. PMID 23745795.

[4] Richards SEV and Hooser SDV, 2018. Neural architecture: from cells to circuits. *J Neurophysiol* **120** (2): 854–866. PMID 29766767.

[5] Ahrens MB, Orger MB, Robson DN, Li JM, and Keller PJ, 2013. Whole-brain functional imaging at cellular resolution using light-sheet microscopy. *Nat Methods* **10** (5): 413–420. PMID 23524393.

[6] Zheng Z, Lauritzen JS, Perlman E, Robinson CG, Nichols M, Milkie D, Torrens O, Price J, Fisher CB, Sharifi N, Calle-Schuler SA, Kmecova L, Ali IJ, Karsh B, Trautman ET, Bogovic JA, Hanslovsky P, Jefferis GSXE, Kazhdan M, Khairy K, Saalfeld S, Fetter RD, and Bock DD, 2018. A Complete Electron Microscopy Volume of the Brain of Adult Drosophila melanogaster. *Cell* **174** (3): 730–743. PMID 30033368.

[7] Wanner AA, Kirschmann MA, and Genoud C, 2015. Challenges of microtome-based serial block-face scanning electron microscopy in neuroscience. *J Microsc* **259** (2): 137–142. PMID 25907464.

[8] Kulkarni RU and Miller EW, 2017. Voltage Imaging: Pitfalls and Potential. *Biochemistry* **56** (39): 5171–5177. PMID 28745864.

[9] Kubota Y, Sohn J, and Kawaguchi Y, 2018. Large Volume Electron Microscopy and Neural Microcircuit Analysis. *Front Neural Circuits* **12**: 98. PMID 30483066.

[10] Miller EW, Lin JY, Frady EP, Steinbach PA, Kristan WB Jr, and Tsien RY, 2012. Optically monitoring voltage in neurons by photo-induced electron transfer through molecular wires. *Proc Natl Acad Sci U S A* **109** (6): 2114–2119. PMID 22308458.

[11] Tomina Y and Wagenaar DA, 2017. A double-sided microscope to realize whole-ganglion imaging of membrane potential in the medicinal leech. *Elife* **6**: e29839. PMID 28944754.

[12] Pipkin JE, Bushong EA, Ellisman MH, and Kristan WB Jr, 2016. Patterns and distribution of presynaptic and postsynaptic elements within serial electron microscopic reconstructions of neuronal arbors from the medicinal leech *Hirudo verbana*. *J Comp Neurol* **524** (18): 3677–3695. PMID 27636374.

[13] Jiao ZF, Shang CF, Wang YF, Yang Z, Yang C, Li FN, Xie JZ, Pan JW, Fu L, and Du JL, 2018. All-optical imaging and manipulation of whole-brain neuronal activities in behaving larval zebrafish. *Biomed Opt Express* **9** (12): 6154–6169. PMID 31065420.

[14] Bates AS, Schlegel P, Roberts RJV, Drummond N, Tamimi IFM, Turnbull R, Zhao X, Marin EC, Popovici PD, Dhawan S, Jamasb A, Javier A, Li F, Rubin GM, Waddell S, Bock DD, Costa M, and Jefferis GSXE, 2020. Complete connectomic reconstruction of olfactory projection neurons in the fly brain. *Biorxiv*: https://doi.org/10.1101/2020.01.19.911453.

[15] Xu CS, Januszewski M, Lu Z, Takemura SY, Hayworth KJ, Huang G, Shinomiya K, Maitin-Shepard J, Ackerman D, Berg S, Blakely T, Bogovic J, Clements J, Dolafi T, Hubbard P, Kainmueller D, Katz W, Kawase T, Khairy KA, Leavitt L, Li PH, Lindsey L, Neubarth N, Olbris DJ, Otsuna H, Troutman ET, Umayam L, Zhao T, Ito M, Goldammer J, Wolff T, Svirskas R, Schlegel P, Neace ER, Knecht CJ Jr, Alvarado CX, Bailey DA, Ballinger S, Borycz JA, Canino BS, Cheatham N, Cook M, Dreher M, Duclos O, Eubanks B, Fairbanks K, Finley S, Forknall N, Francis A, Hopkins GP, Joyce EM, Kim SJ, Kirk NA, Kovalyak J, Lauchie SA, Lohff A, Maldonado C, Manley EA, McLin S, Mooney C, Ndama M, Ogundeyi O, Okeoma N, Ordish C, Padilla N, Patrick C, Paterson T, Phillips EE, Phillips EM, Rampally N, Ribeiro C, Robertson MK, Rymer JT, Ryan SM, Sammons M, Scott AK, Scott AL, Shinomiya A, Smith C, Smith K, Smith NL, Sobeski MA, Suleiman A, Swift J, Takemura S, Talebi I, Tarnogorska D, Tenshaw E, Tokhi T, Walsh JJ, Yang T, Horne JA, Li F, Parekh R, Rivlin PK, Jayaraman V, Ito K, Saalfeld S, George R, Meinertzhagen I, Rubin GM, Hess HF, Scheffer LK, Jain V, and Plaza SM, 2020. A connectome of the adult Drosophila central brain. *Biorxiv*: https://doi.org/10.1101/2020.01.21.911859.

[16] Maniates-Selvin JT, Hildebrand DGC, Graham BJ, Kuan AT, Thomas LA, Nguyen T, Buhmann J, Azevedo AW, Shanny BL, Funke J, Tuthill JC, and Lee WCA, 2020. Reconstruction of motor control circuits in adult Drosophila using automated transmission electron microscopy. *Biorxiv*: https://doi.org/10.1101/2020.01.10.902478.

[17] Hildebrand DGC, Cicconet M, Torres RM, Choi W, Quan TM, Moon J, Wetzel AW, Champion AS, Graham BJ, Randlett O, Plummer GS, Portugues R, Bianco IH, Saalfeld S, Baden AD, Lillaney K, Burns R, Vogelstein JT, Schier AF, Lee WA, Jeong WK, Lichtman JW, and Engert F, 2017. Whole-brain serial-section electron microscopy in larval zebrafish. *Nature* **545** (7654): 345–349. PMID 28489821.

[18] Bhattacharya A, Aghayeva U, Berghoff EG, and Hobert O, 2019. Plasticity of the Electrical Connectome of C. elegans. *Cell* **176** (5): 1174–1189. PMID 30686580.

[19] Grinvald A and Hildesheim R, 2004. VSDI: a new era in functional imaging of cortical dynamics. *Nature Rev Neurosci* **5** (11): 874–885. PMID 15496865.

[20] Harris KM, Perry E, Bourne J, Feinberg M, Ostroff L, and Hurlburt J, 2006. Uniform serial sectioning for transmission electron microscopy. *J Neurosci* **26** (47): 12101–12103. PMID 17122034.

[21] Kristan WB Jr, Calabrese RL, and Friesen WO, 2005. Neuronal control of leech behavior. *Prog Neurobiol* **76** (5): 279–327. PMID 16260077.

[22] Briggman KL, Abarbanel HDI, and Kristan WB, 2005. Optical imaging of neuronal populations during decision-making. *Science* **307** (5711): 896–901. PMID 15705844.

[23] Muller KJ, Nicholls JG, and Stent GS (eds.), 1981. *Neurobiology of the leech*. Cold Spring Harbor Laboratory Press, Cold Spring Harbor, NY.

[24] Wagenaar DA, 2015. A classic model animal in the 21st century: recent lessons from the leech nervous system. *J Exp Biol* **218** (21): 3353–3359. PMID 26538172.

[25] Macagno ER, 1980. Number and distribution of neurons in leech segmental ganglia. *J Comp Neurol* **190** (2): 283–302. PMID 7381060.

[26] Muller KJ and McMahan UJ, 1976. The shapes of sensory and motor neurones and the distribution of their synapses in ganglia of the leech: a study using intracellular injection of horseradish peroxidase. *Proc Roy Soc Lond B* **194** (1117): 481–499. PMID 12513.

[27] Fan RJ, Marin-Burgin A, French KA, and Friesen WO, 2005. A dye mixture (Neurobiotin and Alexa 488) reveals extensive dye-coupling among neurons in leeches; physiology confirms the connections. *J Comp Physiol A* **191** (12): 1157–1171. PMID 16133497.

[28] Wagenaar DA, 2017. An interactive map of the segmental ganglia of *Hirudo verbana*. URL `http://wagenaarlab.caltech.edu/ganglion`, retrieved Feb 10, 2020.

[29] Takahashi N, Kitamura K, Matsuo N, Mayford M, Kano M, Matsuki N, and Ikegaya Y, 2012. Locally synchronized synaptic inputs. *Science* **335** (6066): 353–356. PMID 22267814.

[30] Varga Z, Jia H, Sakmann B, and Konnerth A, 2011. Dendritic coding of multiple sensory inputs in single cortical neurons in vivo. *Proc Natl Acad Sci U S A* **108** (37): 15420–15425. PMID 21876170.

[31] Druckmann S, Feng L, Lee B, Yook C, Zhao T, Magee JC, and Kim J, 2014. Structured synaptic connectivity between hippocampal regions. *Neuron* **81** (3): 629–640. PMID 24412418.

[32] Stent GS, Kristan WB Jr, Friesen WO, Ort CA, Poon M, and Calabrese RL, 1978. Neuronal generation of the leech swimming movement. *Science* **200** (4348): 1348–1357. PMID 663615.

[33] Norris BJ and Calabrese RL, 1987. Identification of motor neurons that contain a FMRFamide-like peptide and the effects of FMRFamide on longitudinal muscle in the medicinal leech, *Hirudo medicinalis*. *J Comp Neurol* **266** (1): 95–9111. PMID 3323268.

[34] Ort CA, Kristan WB, and Stent GS, 1974. Neuronal control of swimming in medicinal leech. 2. Identification and connections of motor neurons. *J Comp Physiol* **94** (2): 121–154.

[35] Shu X, Lev-Ram V, Deerinck TJ, Qi Y, Ramko EB, Davidson MW, Jin Y, Ellisman MH, and Tsien RY, 2011. A genetically encoded tag for correlated light and electron microscopy of intact cells, tissues, and organisms. *PLoS Biol* **9** (4): e1001041. PMID 21483721.

[36] Briggman KL and Kristan WB, 2008. Multifunctional pattern-generating circuits. *Annu Rev Neurosci* **31**: 271–294. PMID 18558856.

[37] Fu M, Yu X, Lu J, and Zuo Y, 2012. Repetitive motor learning induces coordinated formation of clustered dendritic spines in vivo. *Nature* **483** (7387): 92–95. PMID 22343892.

[38] Kleindienst T, Winnubst J, Roth-Alpermann C, Bonhoeffer T, and Lohmann C, 2011. Activity-dependent clustering of functional synaptic inputs on developing hippocampal dendrites. *Neuron* **72** (6): 1012–1024. PMID 22196336.

[39] Plaza SM and Funke J, 2018. Analyzing Image Segmentation for Connectomics. *Front Neural Circuits* **12**: 102. PMID 30483069.

[40] Alivisatos AP, Chun M, Church GM, Greenspan RJ, Roukes ML, and Yuste R, 2012. The brain activity map project and the challenge of functional connectomics. *Neuron* **74** (6): 970–974. PMID 22726828.

[41] Denk W, Briggman KL, and Helmstaedter M, 2012. Structural neurobiology: missing link to a mechanistic understanding of neural computation. *Nature Rev Neurosci* **13** (5): 351–358. PMID 22353782.

[42] Bargmann CI and Marder E, 2013. From the connectome to brain function. *Nat Methods* **10** (6): 483–490.

[43] Morgan JL and Lichtman JW, 2013. Why not connectomics? *Nat Methods* **10** (6): 494–500. PMID 23722208.

[44] Devor A, Bandettini PA, Boas DA, Bower JM, Buxton RB, Cohen LB, Dale AM, Einevoll GT, Fox PT, Franceschini MA, Friston KJ, Fujimoto JG, Geyer MA, Greenberg JH, Halgren E, Hamalainen MS, Helmchen F, Hyman BT, Jasanoff A, Jernigan TL, Judd LL, Kim SG, Kleinfeld D, Kopell NJ, Kutas M, Kwong KK, Larkum ME, Lo EH, Magistretti PJ, Mandeville JB, Masliah E, Mitra PP, Mobley WC, Moskowitz MA, Nimmerjahn A, Reynolds JH, Rosen BR, Salzberg BM, Schaffer CB, Silva GA, So PT, Spitzer NC, Tootell RB, Essen DCV, Vanduffel W, Vinogradov SA, Wald LL, Wang LV, Weber B, and Yodh AG, 2013. The challenge of connecting the dots in the B.R.A.I.N. *Neuron* **80** (2): 270–274. PMID 24139032.

[45] Kandel ER, Markram H, Matthews PM, Yuste R, and Koch C, 2013. Neuroscience thinks big (and collaboratively). *Nature Rev Neurosci* **14** (9): 659–664. PMID 23958663.

[46] Wang Z, Chen LM, Negyessy L, Friedman RM, Mishra A, Gore JC, and Roe AW, 2013. The relationship of anatomical and functional connectivity to resting-state connectivity in primate somatosensory cortex. *Neuron* **78** (6): 1116–1126. PMID 23791200.

[47] Tomina Y and Wagenaar DA, 2018. Dual-sided voltage-sensitive dye imaging of leech ganglia. *Bio Protoc* **8** (5): e2751. PMID 29594188.

[48] Woodford CR, Frady EP, Smith RS, Morey B, Canzi G, Palida SF, Araneda RC, Kristan WB Jr, Kubiak CP, Miller EW, and Tsien RY, 2015. Improved PeT molecules for optically sensing voltage in neurons. *J Am Chem Soc* **137** (5): 1817–1824. PMID 25584688.

[49] Walton J, 1979. Lead aspartate, an en bloc contrast stain particularly useful for ultrastructural enzymology. *J Histochem Cytochem* **27** (10): 1337–1342. PMID 512319.

[50] Wetzel AW, Bakal J, Dittrich M, Hildebrand DGC, Morgan HL, and Lichtman JW, 2016. Registering large volume serial-section electron microscopy image sets for neural circuit reconstruction using FFT signal whitening. In *Proc. IEEE Applied Imagery Pattern Recognition Workshop*, 2016.

[51] Google. Neuroglancer: WebGL-based viewer for volumetric data. URL `https://github.com/google/neuroglancer`.

Acknowledgments

We thank Evan Miller for sharing of the VF2.1(OMe).H dye. Tünde Magyar, Renáta Pop at the University of Veterinary Medicine, Department of Anatomy and Histology, in Budapest, Hungary helped with TEM. This work was supported by the National Institute of Neurological Disorders and Stroke (R01NS094403 to DAW) and by the National Institute of General Medical Sciences (P41GM103412 in support of the National Center for Molecular Imaging Research to MHE). YT was supported by Japan Society for Promotion of Science (Overseas Research Fellowship, Research Fellowship for Young Scientists PD, 201800526 and Grant-in-Aid for Young Scientists, 19K16191). PKF was supported by the Swiss National Science Foundation (P2EZP3_181896).

Author information

Conceptualization: YT, PKF, MHE, WBK, DAW
Data curation: YT, DAW
Formal analysis: YT, MA, PKF, DAW
Funding acquisition: YT, PKF, MHE, WBK, DAW
Investigation: YT, MA, PKF, EAB
Methodology: All
Software: PKF, DAW
Supervision: MHE, DAW
Visualization: YT, MA, PKF, DAW
Writing—original draft: YT, MA
Writing—review and editing: YT, MA, PKF, DAW

Ethics declarations

The authors declare no competing interests.

Extended data figures and tables

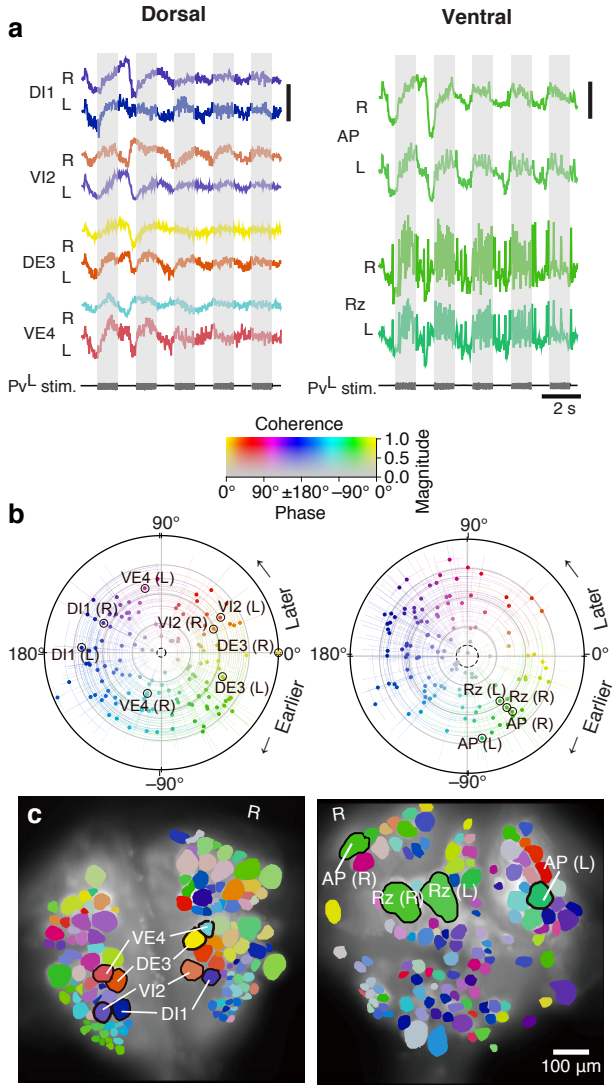

Figure S1: Fictive local bending imaged using VSD. **a**. Selected VSD traces during fictive local bending. From the dorsal surface: dorsal and ventral inhibitory and excitatory motor neurons DI-1, VI-2, DE-3, and VE-4; from the ventral surface: AP cells (well-known postsynaptic partners of the P cells with unknown function) and the Retzius cells. Vertical scale bars: 0.2% relative fluorescence change. **b**. Magnitude (radial axis from 0 to 1) and phase (angular coordinate) of the coherence of activity in individual neurons with the local bend rhythm. Error bars indicate confidence intervals based on a multi-taper estimate. **c**. Coherence maps of the VSD signals of all cells on the dorsal (*left*) and ventral (*right*) surfaces of the ganglion. Colors of cell bodies indicate coherence relative to DE-3^{R}. "R" indicates the right side of the ganglion (i.e., the animal's right when dorsal side up). Color scale applies to all panels.

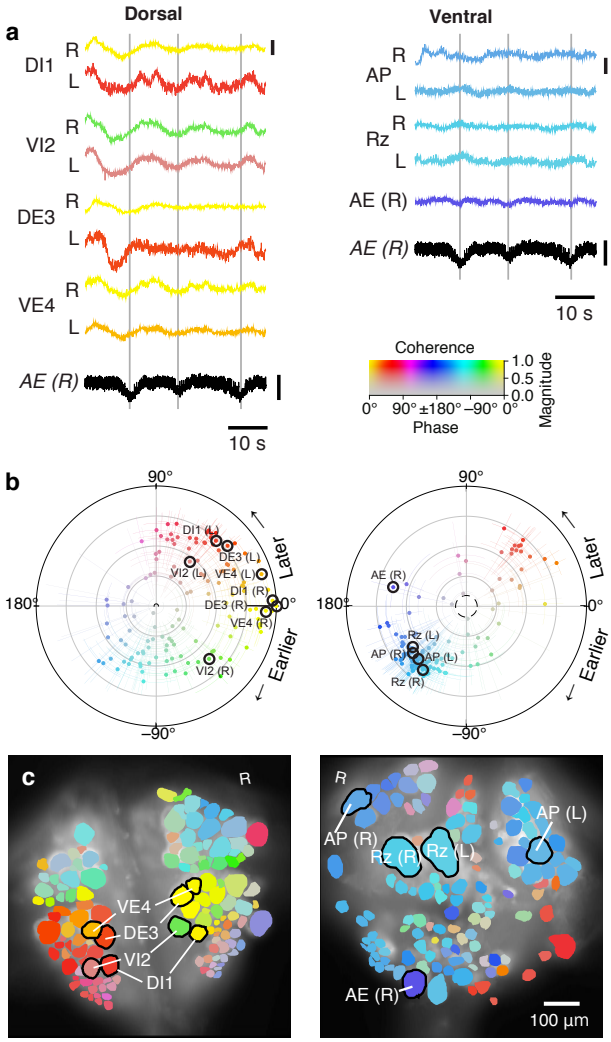

Figure S2: Fictive crawling imaged using VSD. **a**. Selected VSD traces during fictive crawling. From the dorsal surface: dorsal and ventral inhibitory and excitatory motor neurons DI-1, VI-2, DE-3, and VE-4; from the ventral surface: the AP and Retzius cells. Vertical scale bars: 0.2%. Below the traces, a simultaneously recorded intracellular trace of motor neuron AE(R) is displayed (in both columns). Scale bar: 10 mV. Gray bars mark hyperpolarized phase of AE(R). **b**. Magnitude (radial axis from 0 to 1) and phase (angular coordinate) of the coherence of activity in individual neurons with the crawl rhythm. Error bars indicate confidence intervals based on a multi-taper estimate. **c**. Coherence maps of the VSD signals of all cells on the dorsal (*left*) and ventral (*right*) surfaces of the ganglion. Colors of cell bodies indicate coherence relative to DE-3^{R}. "R" indicates the right side of the ganglion (i.e., the animal's right when dorsal side up). Color scale applies to all panels.

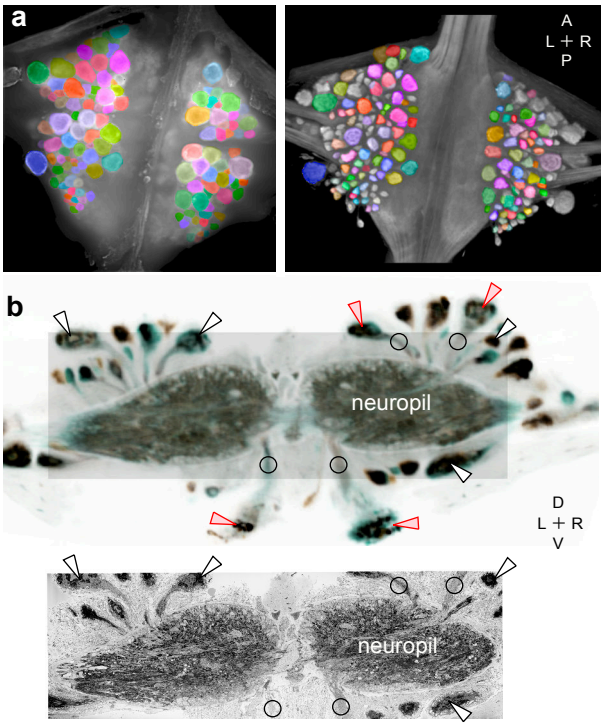

Figure S3: Mapping between functional and anatomical images. **a**. Light micrograph (*left*) and x-ray image (*right*) of the ganglion in which we recorded neuronal activity using a VSD. Like colors label the same cells on the two images. A: Anterior, P: Posterior, L: Left, R: Right. **b**. Transverse section from X-ray tomographic image stack of the ganglion (*top*). Only the shaded area was imaged with SBEM (*bottom*). Arrowheads mark several somata that are (*white*) or are not (*red*) included in the SBEM volume. Circles mark neurites that facilitate complete mapping between the two imaging modalities. D: Dorsal, V: Ventral.

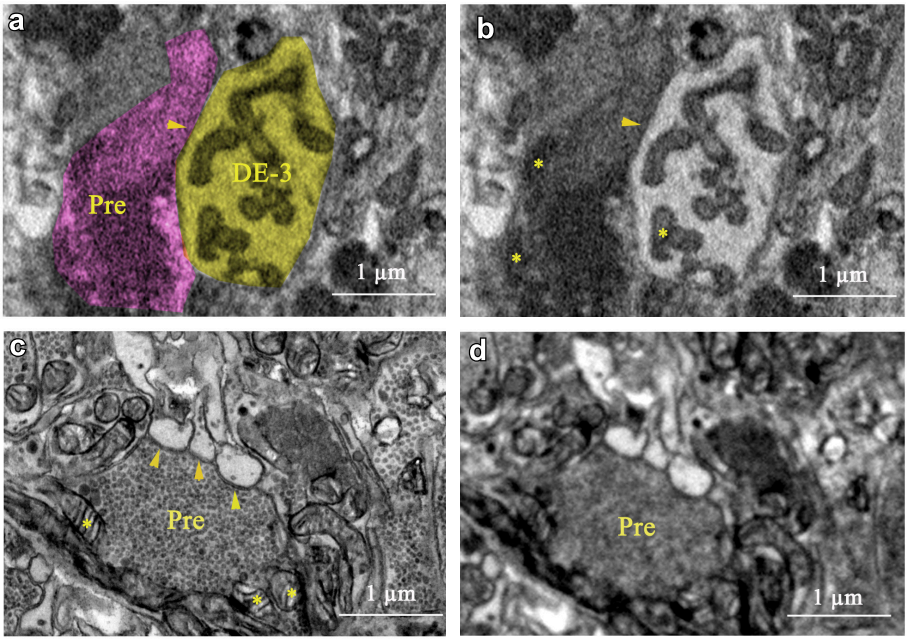

Figure S4: Comparison of SEM with TEM for interpreting synapses. **a**. Our interpretation of a small section of our SBEM image: a process of cell DE-3 (*yellow*) and a presynaptic partner (*purple*). **b**. Same area without overlay. Arrowhead: synapse. Stars: Mitochondria. **c**. A similar area imaged with TEM (from a ganglion from another leech). **d**. Same area as (c), computationally blurred to simulate the lower resolving power of SEM.

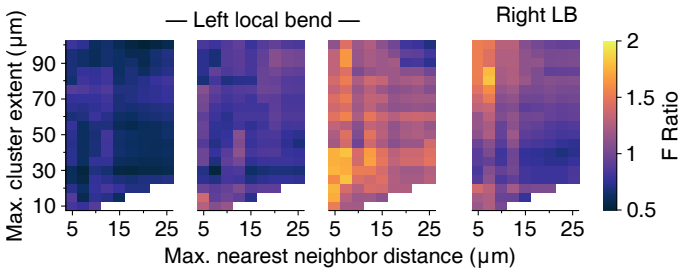

Figure S5: Clustering results for the local bend trials. Out of the four trials, the first three involved stimulation of the left P_V cell; the final trial involved stimulation of the right P_V cell. In contrast to the swim and crawl trials (4c), the clustering results for local bend trials are inconsistent.

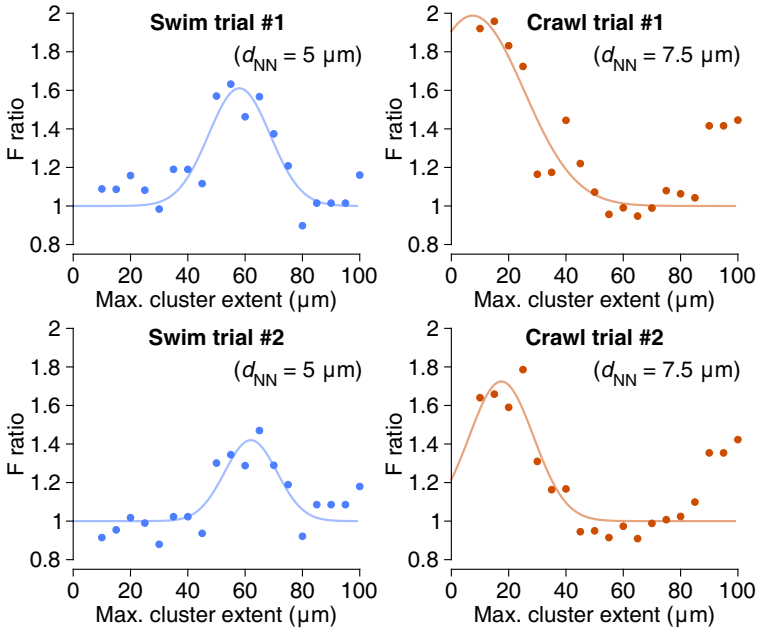

Figure S6: Peak F-ratios for connecting spatial clusters to functional activity. These graphs represent slices through the data shown in Fig. 4c, vertically through the highest peak in the parameter space. Lines are Gaussians fitted through the data; see Methods.

Supplementary information

Clustering results

Trial	$(d_{\mathrm{NN}}, e_{\mathrm{C}})$	F-ratio	p-value
Swim trial 1	(5, 50)	1.57	0.031
Swim trial 1	(5, 55)	1.632	0.028
Swim trial 1	(5, 60)	1.463	0.028
Swim trial 1	(5, 65)	1.567	0.032
Swim trial 1	(7.5, 65)	1.435	0.027
Swim trial 2	(5, 65)	1.47	0.041

Table S1: Results of the ANOVA analysis of synaptic clusters in swim trials. Shown are at most 10 of the pairs of parameter values that yielded significant results ($p < 0.05$). Parameter values are expressed in µm.

Trial	$(d_{\mathrm{NN}}, e_{\mathrm{C}})$	F-ratio	p-value
Crawl trial 1	(10, 15)	1.672	0.038
Crawl trial 1	(10, 20)	1.594	0.04
Crawl trial 1	(7.5, 15)	1.958	0.038
Crawl trial 1	(7.5, 10)	1.92	0.04
Crawl trial 1	(7.5, 20)	1.831	0.038
Crawl trial 1	(7.5, 25)	1.724	0.04
Crawl trial 1	(10, 15)	1.673	0.028
Crawl trial 1	(10, 20)	1.594	0.034
Crawl trial 1	(12.5, 15)	1.533	0.028
Crawl trial 1	(12.5, 20)	1.491	0.034
Crawl trial 2	(7.5, 25)	1.786	0.028
Crawl trial 2	(7.5, 15)	1.659	0.03
Crawl trial 2	(7.5, 10)	1.640	0.029
Crawl trial 2	(7.5, 20)	1.59	0.031
Crawl trial 2	(10, 25)	1.469	0.038
Crawl trial 2	(7.5, 100)	1.423	0.035
Crawl trial 2	(12.5, 30)	1.415	0.037

Table S2: Results of the ANOVA analysis of synaptic clusters, crawl trials.

Trial	$(d_{\mathrm{NN}}, e_{\mathrm{C}})$	F-ratio	p-value
Local bend trial 1	(5, 15)	1.37	0.048
Local bend trial 2	(5, 15)	1.726	0.036
Local bend trial 2	(5, 20)	1.756	0.03
Local bend trial 2	(5, 25)	1.751	0.03
Local bend trial 2	(5, 30)	1.735	0.031
Local bend trial 2	(5, 35)	1.735	0.021
Local bend trial 2	(5, 40)	1.735	0.021
Local bend trial 2	(7.5, 25)	1.8	0.042
Local bend trial 2	(7.5, 30)	1.722	0.042
Local bend trial 2	(7.5, 35)	1.714	0.042
Local bend trial 2	(7.5, 40)	1.805	0.038
Local bend trial 3	(5, 80)	1.52	0.039
Local bend trial 3	(5, 85)	1.525	0.039
Local bend trial 3	(5, 90)	1.525	0.037
Local bend trial 3	(5, 95)	1.525	0.04
Local bend trial 3	(5, 100)	1.526	0.037
Local bend trial 3	(7.5, 70)	1.502	0.038
Local bend trial 3	(7.5, 75)	1.591	0.034
Local bend trial 3	(7.5, 80)	1.807	0.018
Local bend trial 3	(7.5, 85)	1.768	0.022
Local bend trial 3	(7.5, 100)	1.495	0.033

Table S3: Results of the ANOVA analysis of synaptic clusters, local bend trials.